RSC Advances

Journal Name

ARTICLE TYPE

LiV$_3$O$_8$ nanorods as cathode materials for high-power and long-life rechargeable lithium-ion batteries

Peng Mei,[a,b] Xing-Long Wu,*[a,b] Haiming Xie,[a,b] Liqun Sun,[a,b] Yanping Zeng,[a,b] Jingping Zhang,*[a] Linghua Tai,[a,b] Xin Guo,[a,b] Lina Cong,[a,b] Shunchao Ma,[a,b] Cen Yao,[a,b] and Rongshun Wang*[a,b]

Nowadays one of the principal challenges for lithium-ion batteries (LIBs) lies in fulfilling the burgeoning demands for high energy and power density with long cycle life. Herein, we demonstrate a two-step route for synthesizing LiV$_3$O$_8$ nanorods with confined preferential orientation by using self-made VO$_2$(B) 10 nanosheets as the precursor. The special structures of nanorods endue the LiV$_3$O$_8$ materials with markedly enhanced reversible capacities, prominent high-rate capability and long-term cyclability as cathodes for lithium storage. The results disclosed that, much desirable initial capacities of 161 and 158 mA h g^{-1} can be achieved for the LiV$_3$O$_8$ nanorods at extremely high rates of 2000 and 3000 mA g^{-1}, with minimal capacity loss of 0.037% and 0.031% per cycle throughout the lasting 300 and 500 cycles, respectively. 15 The energetically optimized electron conduction and lithium diffusion kinetics in electrode process may shed light on the superior electrochemical properties of the LiV$_3$O$_8$ nanorods, primarily benefitting from the small particle size, large surface area and restricted preferential ordering along (100) plane.

Introduction

In response to the critical needs of modern society and rising 20 ecological concerns, it is pressing to explore alternative sustainable and eco-friendly energy/power source.[1,2] As efficient, light-weight, and rechargeable power sources, lithium-ion batteries (LIBs) are deemed to be one of the most promising candidates for future energy storage and conversion. 25 Rechargeable LIBs have revolutionized diverse portable electronic devices over the past two decades.[3,4] However, the next market opportunities will be much tougher for current state-of-art LIBs to conquer, as the emerging applications (such as hybrid electric vehicles (HEVs), electrical vehicles (EV)) mostly 30 require high energy and high power density (i.e., the ability to stand quick charge and discharge with high current density). Therefore, electrode materials possessing high reversible Li storage capacity and rapid solid-state lithium-ion and electron transport are indispensable to achieve the increase in energy and 35 power density to meet the increasing needs of energy storage.[5-8]

Lithium trivanadate (LiV$_3$O$_8$) with monoclinic structure has been widely studied as a cathode material for LIBs due to its good features such as high specific capacity, good structural stability, low cost and desirable safety.[9-18] Theoretically LiV$_3$O$_8$ 40 crystalline electrode can accommodate additional three lithium ions per formula unit without any structural damage, equivalent to a capacity of *ca.* 280 mA h g^{-1}, which is much higher than that of current available cathode materials (such as LiCoO$_2$ and LiFePO$_4$). It has been demonstrated that the electrochemical 45 properties of LiV$_3$O$_8$ show strong dependence on its preparation method as well as the particle size, morphology and crystalline

texture formed.[19] In this regard, several methods have been developed to improve the electrochemical performance of LiV$_3$O$_8$ cathode materials, including microwave synthesis,[20] sol-gel 50 method,[19] spray drying,[21] low-temperature synthesis,[22] hydrothermal method,[23] ultrasonic preparation,[24] etc. Enhanced Li storage capacity and rate performance have been realized by morphological control of nanostructured LiV$_3$O$_8$,[11,25,26] while the capacity retention and high-rate capability with long cycle life 55 still need to be further improved to satisfy the practical high-power applications.

The exploitation of electrode materials with nanostructure is regarded as one of the most favorable approaches towards achieving these goals. Nanomaterials could play a significant role 60 in improving the Li storage capacity and electrode kinetics as well as cyclic stability in a lithium-ion battery system, owing to the short distance for rapid transport of both lithium ions and electrons, and huge surface area, which reduces the overpotential and permits faster reaction kinetics at the electrode surface.[6,27-29] 65 Herein, we report a nanorod-structured LiV$_3$O$_8$ with restricted preferential orientation synthesized through a two-step route using self-made VO$_2$(B) nanosheets as the precursor. Benefitting from the nanometer size effects, much enhanced Li storage capacity, enormously improved high-rate performance and 70 impressive long-cycle stability have been achieved for the LiV$_3$O$_8$ nanorods.

Experimental section

Preparation of nanostructured VO$_2$(B) precursor

Nanostructured VO$_2$(B) precursor was firstly fabricated via a

hydrothermal method. Analytically pure V_2O_5 and $C_2H_2O_4 \cdot 2H_2O$ were used as starting material. V_2O_5 powder was dissolved in vigorously stirred oxalic acid aqueous solution at gentle temperature until a blue solution formed. Subsequently, the resulting solution was transferred to a Teflon-sealed stainless steel autoclave and stored at 180°C for 24 h in an oven. The precipitate was separated through a high-velocity centrifuge, washed with de-ionized water and anhydrous ethanol for several times and then dried at 70°C overnight.

Synthesis of LiV₃O₈ samples

In a typical synthesis, an appropriate amount of the as-obtained $VO_2(B)$ precursor was added to alcoholic solution of lithium hydroxide (the molar ratio of V/Li was 3/1.05) with vigorous stirring, and kept for 2 h to obtain a homogeneous mixture. In succession, the solvent was distilled off via a rotary evaporator. The collected powder was then annealed in air at 500°C for 8 h, and the LiV_3O_8 nanorods obtained were denoted as n-LVO hereafter. For comparison, bulk LiV_3O_8 materials were prepared by the similar procedure using commercial VO_2 as precursor (this bulk sample was designated as b-LVO).

Characterization

The chemical compositions and crystallographic information of the as-synthesized samples were collected by Powder X-ray diffraction (XRD) with a Bruker D8 Advanced diffractometer using Cu Kα (λ = 1.5406 Å) radiation. The morphology and microstructure of the as-prepared materials were characterized by scanning electron microscope (Philips XL 30 and JEOL JSM-6700F Field Emission, 10 kV), transmission electron microscopy (TEM), and high-resolution TEM (JEOL-2100 F, 200 kV). The Brunauer-Emmett-Teller (BET) specific surface area of the products was determined by utilizing an ASAP 2020 using the standard N_2 adsorption and desorption isotherm measurements at 77 K, after degassing the powder samples at 150°C for 8 h in vacuum. The electrochemical properties were investigated with 2025 coin cells assembled in a glove box (Mbraun, Inc.) filled with pure argon gas. The working electrode was fabricated by casting the slurry (70 wt% of active materials, 20 wt% of acetylene black, and 10 wt% of polyvinylidene fluoride (PVDF) binder in *N*-methyl-2-pyrrolidinone (NMP)) onto Al foil, and then dried in a vacuum oven at 120°C for 12 h to remove the solvent. Lithium foil was employed as the counter electrode and 1 M $LiPF_6$ in ethylene carbonate/dimethyl carbonate (EC/DMC) (1/1 by volume) was used as the electrolyte. The charge/discharge performances of the electrodes were evaluated at room temperature using a multichannel battery testing system (LAND CT2001A). The cyclic voltammetry (CV) tests were carried out on a CHI660E electrochemical workstation (Shanghai CHI Instrument Company, China) with lithium foil as both the counter and reference electrode over the potential range of 1.5-4.0 V (*vs.* Li^+/Li) at the scanning rate of 0.5 mV s⁻¹. The electrochemical impedance spectroscopy (EIS) investigation was implemented by a Princeton Applied Research PARSTAT 2273 advanced electrochemical system in the frequency range from 200 kHz to 0.01 Hz with an applied perturbation signal of 5 mV.

Results and discussion

Structural characterization

The chemical composition and phase structure of the as-synthesized $VO_2(B)$ precursor were identified via XRD, with the result shown in Fig. 1a. The XRD pattern can be readily assigned to the monoclinic crystalline $VO_2(B)$ (space group: *C2/m*, JCPDS 31-1438). No obvious diffraction peaks of any other impurities were detected in the spectrum, indicative of high phase purity of the precursor. Fig. 1b presents a representative SEM image of as-prepared $VO_2(B)$ materials. The SEM observation distinctly shows that the $VO_2(B)$ precursor consists of uniformly sheet-like nanoparticles with an average thickness of about 25 nm and several hundreds of nanometers in length. The TEM image shown in Fig. 1c further validates that the $VO_2(B)$ nanosheets are typically of 50-80 nm wide and 400-600 nm long. Further inspection using high-resolution TEM (HRTEM) (Fig. 1d) discloses the well-resolved lattice fringes with an interplanar distance of 0.578 nm, in accordance with the spacing of the (200) planes of $VO_2(B)$. The corresponding Fast Fourier Transform (FFT) pattern (the inset of Fig. 1d) displays a regular spot pattern, further affirming the single-crystal nature of these nanosheets.
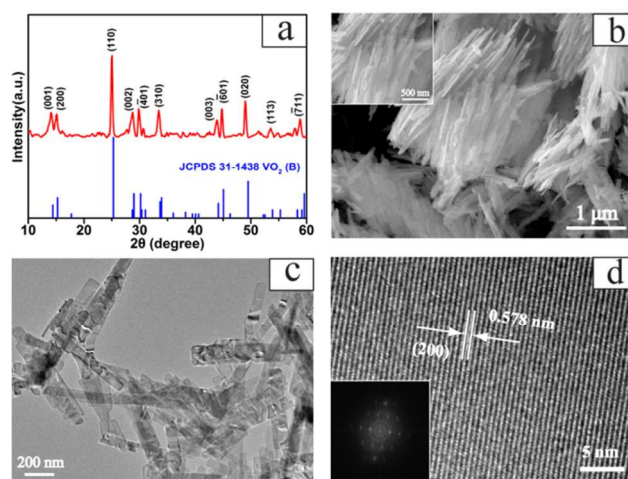
Fig. 1 Characterizations of $VO_2(B)$ nanosheets precursor, (a) XRD pattern; (b) SEM image; (c) TEM image; (d) HRTEM image and the corresponding FFT pattern (lower-left inset).
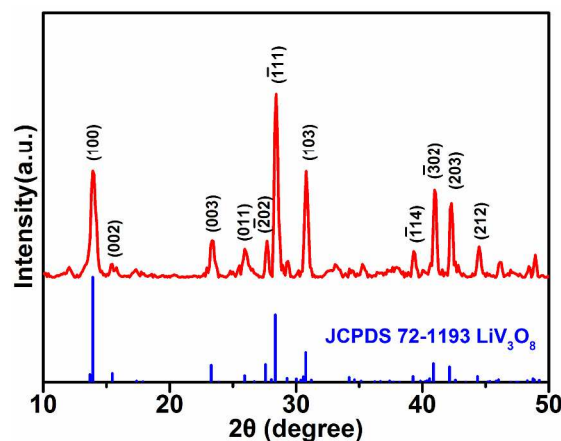
Fig. 2 XRD pattern of LiV_3O_8 nanorods

The XRD pattern of the LiV_3O_8 (n-LVO) fabricated by the $VO_2(B)$ precursor is shown in Fig. 2. The main distinct diffractive peaks can be easily ascribed to the known monoclinic LiV_3O_8

(space group: $P2_1/m$, JCPDS 72-1193). The peak located at around 14° belongs to diffraction at the (100) plane, implying the layered-type structure of crystallized LiV_3O_8. As illustrated in Fig. 3, the crystalline structure of LiV_3O_8 is comprised of $[V_3O_8]$ layers developed in the *bc* plane, and stacked along the *a* axis. It should be pointed out that, the diffraction intensity of crystal plane (100) is obviously lower than that of ($\overline{1}$11) in the present n-LVO system, which is opposite to that in the standard XRD pattern and common results reported in the literatures.[11, 15, 17, 30, 31] That further demonstrates the oriented structure characteristic of the n-LVO, in accordance with the SEM and TEM observations. It can be rationally inferred that the oriented growth of n-LVO may be originated from the one-dimensional characteristic of $VO_2(B)$ precursor, which would restrict the growth of <100> direction in the transition process from $VO_2(B)$ to LiV_3O_8 and finally result in the formation of LiV_3O_8 nanorods. For the LiV_3O_8 materials as cathode for LIBs, it has been demonstrated that the reduced dimension of <100> direction can effectively shorten the diffusion distance and time of lithium ions inserted

into and extracted out the LiV_3O_8 crystallites.[14, 19, 32, 33] In the XRD pattern of present n-LVO, the depressed diffraction intensity of (100) crystal plane signifies that the dimension of the crystallites along <100> direction has been evidently reduced.[34] Therefore, it can be deduced that superior electrochemical properties would be achieved for the obtained n-LVO.
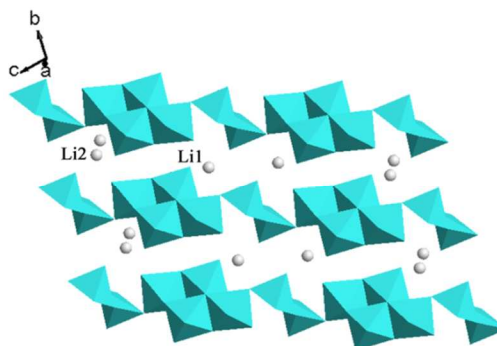
Fig. 3 Projection of the crystalline structure of LiV_3O_8 along the *a* axis.
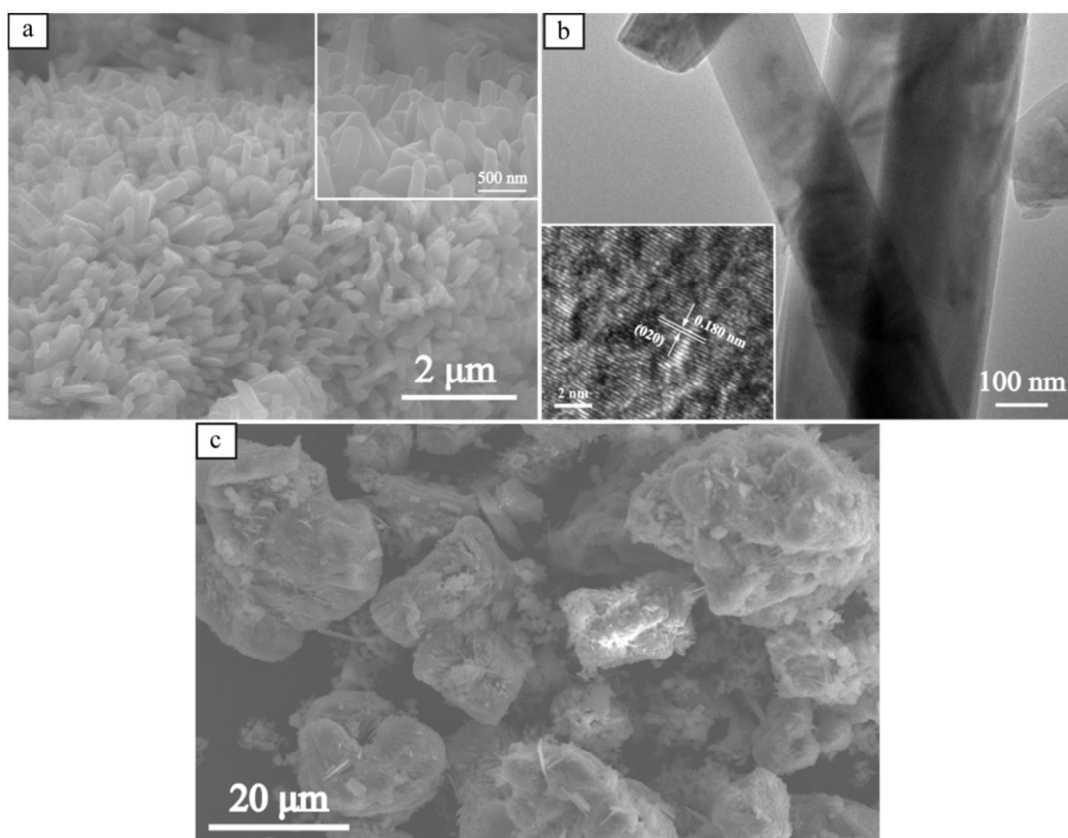
Fig. 4 (a) SEM images of n-LVO; (b) TEM image of n-LVO and its HRTEM image (lower-left inset); (c) SEM image of b-LVO.

The morphologies of the LiV_3O_8 samples prepared from different precursors are further compared by SEM images as shown in Fig. 4. For the LiV_3O_8 sample fabricated by using commercial VO_2 as the raw materials (thereafter abbreviated as b-LVO), it is mainly composed of irregular and inhomogeneous spheroids with the diameter of about 20-35 μm, as the typical SEM image shown in Fig. 4c. In addition, these micrometer-sized LiV_3O_8 particles are severely aggregated, which is unfavorable

for the fabrication of high-performance electrode and the charge/discharge processes. Excitingly, the n-LVO developed presently by using self-made $VO_2(B)$ nanosheets as the precursor exhibits uniform and evenly rod-like structures with 150-300 nm in width and 0.8-1.5 μm in length (Fig. 4a). A proposed mechanism for the evolution of n-LVO is presented in Fig. 5. Under hydrothermal condition, V_2O_5 powders were reduced by oxalic acid and formed VO^{2+}, which consequently self-assembled

into $VO_2(B)$ nanosheets. Then the $VO_2(B)$ was transformed into LiV_3O_8 after lithiation. Presumably the one-dimensional characteristic of $VO_2(B)$ nanosheets had restricted the growth of <100> direction in the transition process and finally resulted in

5 the formation of LiV_3O_8 crystalline with confined preferential orientation. Furthermore, TEM and HRTEM observations are also employed to provide deeper insight into the microstructure of n-LVO. A closer look on the n-LVO in Fig. 4b indicates that dimensions of the nanorods agree well with the SEM observation.

10 The n-LVO partially preserves the shape of self-made $VO_2(B)$ precursor, while the dimensions have grown larger after lithiation. It could be rationally reduced that the nanorod-like structure of n-LVO derived from the heat-temperature process (500°C, 8h), in which $VO_2(B)$ nanosheets would tend to aggregate and pack on

15 each other, as well as the chemical reaction process between VO_2 and LiOH, leading to the transition of crystallographic texture. HRTEM image (inset of Fig. 4b) exhibits relatively defined crystalline lattices with the spacing of 0.180 nm, which is in good agreement with the (020) interplanar distance of monoclinic

20 LiV_3O_8 (JCPDS 72-1193). Dramatically shortened transport distance for both electrons and lithium ions is anticipated to be attained for n-LVO due to the significantly reduced grain size relative to b-LVO, which would give a guarantee of full lithium diffusion within a very short period, i.e., at high charge/discharge

25 rates.[4, 7, 35, 36] Moreover, the drastic decrease in dimensions tends to give rise to a significant increase in specific surface area of n-LVO. Calculated from the N_2 adsorption and desorption isotherm (Fig. S2†), the Brunauer-Emmett-Teller (BET) specific surface area of n-LVO is 26.593 $m^2 g^{-1}$, while b-LVO shows a

30 dramatically smaller BET specific surface area of merely 0.1256 $m^2 g^{-1}$. The substantially enlarged specific surface area should not only provide efficient contact of active material with electrolyte and more active sites for lithium diffusion and accommodation, but also considerably reduce overpotential and specific current

35 density of the electrode material, which would promote fast transport of both ions and electrons throughout the electrode matrix.[6, 27-29] Taking all benefits of nanometer size effects into account, it is reasonable to expect the n-LVO to exhibit superior electrochemical properties over the bulk counterpart, especially

40 high-rate performance when they are applied as cathode materials for rechargeable LIBs.
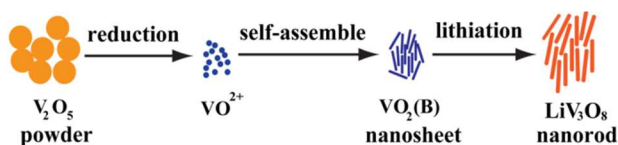
Fig. 5 Schematic illustration of the preparation of LiV_3O_8 nanorods.

Electrochemical characterization

45 To get a rough estimation of the electrochemical behavior of the LiV_3O_8 samples, cyclic voltammetric experiments were conducted at a scan rate of 0.5 mV s^{-1} within a voltage interval of 1.5-4.0 V. The tenth CV curves are shown in Fig. 6. Both CV curves have similar shapes, but differ from each other in the peak

50 location and intensity, i.e., the peak current density. The oxidation and reduction peaks of n-LVO are higher and larger in areas than those of b-LVO, suggesting that the former will deliver higher Li storage capacities and faster kinetics for lithium ions

insertion/extraction in the electrode.[37-40] Furthermore, the voltage

55 separation of n-LVO between the predominant oxidation and reduction peaks (located at around 2.5 V) is found to be eliminated to a large degree compared to that of b-LVO, indicating the deeply optimized electrode kinetics and reversibility of the n-LVO.[33, 41, 42]
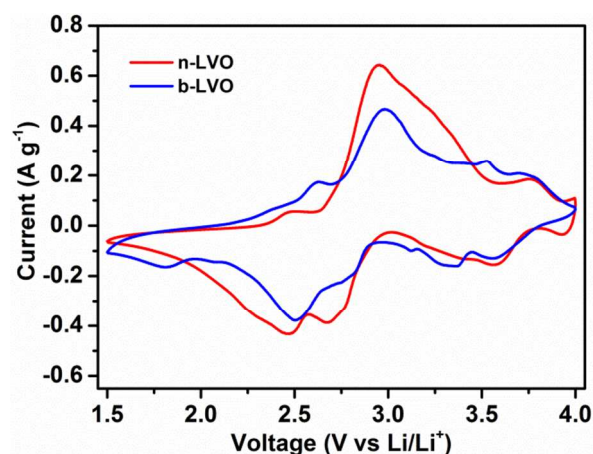
60 **Fig. 6** The tenth cycle CV curves for n-LVO and b-LVO electrodes.
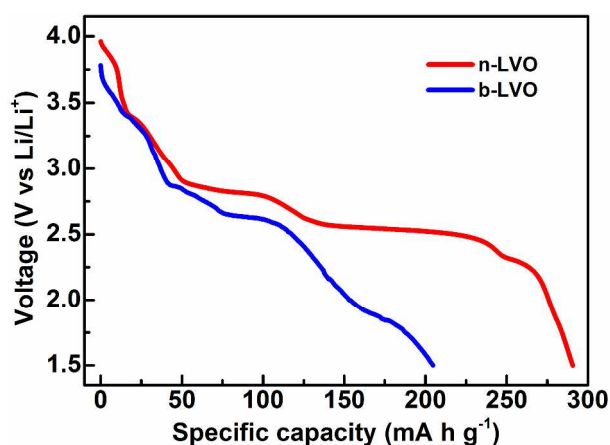
Fig. 7 First-cycle discharge curves of n-LVO and b-LVO electrodes at
65 100 mA g^{-1}.

The initial discharge curves of n-LVO and b-LVO electrodes measured at 100 mA g^{-1} in the range of 1.5-4.0 V (vs. Li^+/Li) are illustrated in Fig. 7. As expected, the n-LVO electrode delivers a desirable initial reversible specific capacity of 290.6 mA h g^{-1},

70 much higher than that of b-LVO (204.6 mA h g^{-1}). In addition, the characteristic multiple discharge plateaus of the former are found to be more easily recognizable. The three evident discharge plateaus located at 2.82 V, 2.53 V and 2.27 V, which coincide well with typical lithium-ion intercalation voltage of LiV_3O_8

75 crystallites as reported in the literatures, can be identified as originating from the single-phase insertion process, the two-phase transformation between $Li_{1+x}V_3O_8$ ($1 \leq x \leq 2$) and $Li_4V_3O_8$, and the slower kinetic insertion process, respectively.[13, 43, 44]

The cycling performances of these LiV_3O_8 electrodes are
80 further compared at a moderately high current density of 600 mA g^{-1} (corresponding to the 2C rate, theoretically), with the results shown in Fig. 8. It shows that both the reversible specific

capacity (Fig. 8a) and capacity retention (Fig. 8b) of the n-LVO are far superior to those of the b-LVO, which should be attributed to the unique nanorod structure of the former. The n-LVO electrode delivers a desirable initial reversible capacity of 200

5 mA h g^{-1} and its capacity well stabilizes at around 190 mA h g^{-1} after 100 cycles, corresponding to as high as 95% of the initial value. In strong contrast, the b-LVO electrode presents a comparatively lower initial reversible capacity of 155.4 mA h g^{-1}, and then decays rapidly to 81.2 mA h g^{-1} after 100 cycles, with a

10 low capacity retention of merely 52%. Most of the LiV_3O_8 crystalline electrodes reported till date can deliver reversible capacities in the range of 125-180 mA h g^{-1} at the same rate of 600 mA g^{-1}.[17, 21, 22, 26, 45-48] Apparently, the as-prepared LiV_3O_8 nanorods have shown enhanced reversible capacity as well as

15 desirable capacity retention at the moderately high current density of 600 mA g^{-1}.
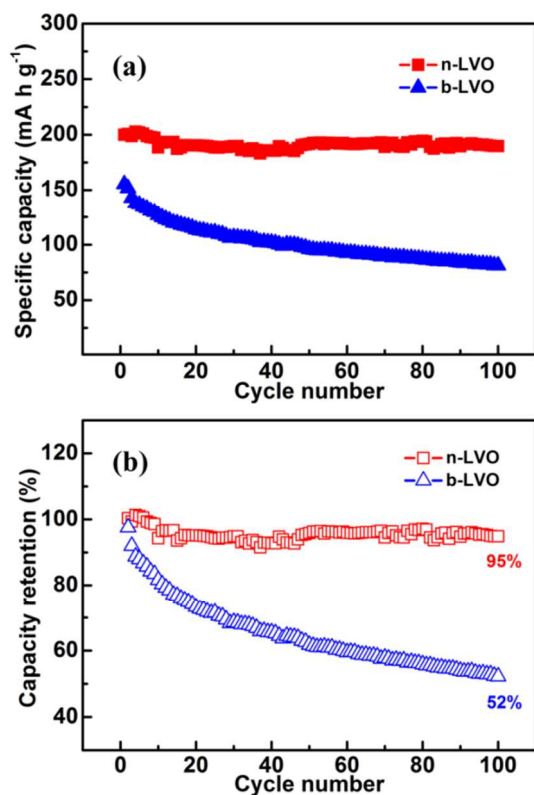
Fig. 8 (a) Cycling performance of n-LVO and b-LVO electrodes at 600 mA g^{-1}, and (b) the corresponding capacity retention plots.

20   To corroborate the anticipated superior rate performance of our LiV_3O_8 nanorods, all batteries were galvanostatic charged and discharged at various current densities that increase stepwise from 100 mA g^{-1} to 1500 mA g^{-1}. The comparative plots of rate performance for the n-LVO and b-LVO electrodes are shown in

25 Fig. 9a. With the current density increasing, the reversible capacities of n-LVO decrease slowly from 291 mA h g^{-1} at 100 mA g^{-1} to 245 and 200 mA h g^{-1} at current densities of 300 and 900 mA g^{-1}, respectively. Notably up to the high rate of 1500 mA g^{-1}, an appreciable reversible capacity of 159 mA h g^{-1} can still be

30 sustained. However, the reversible capacities of most reported LiV_3O_8 crystalline electrodes tested at such high rate usually fall
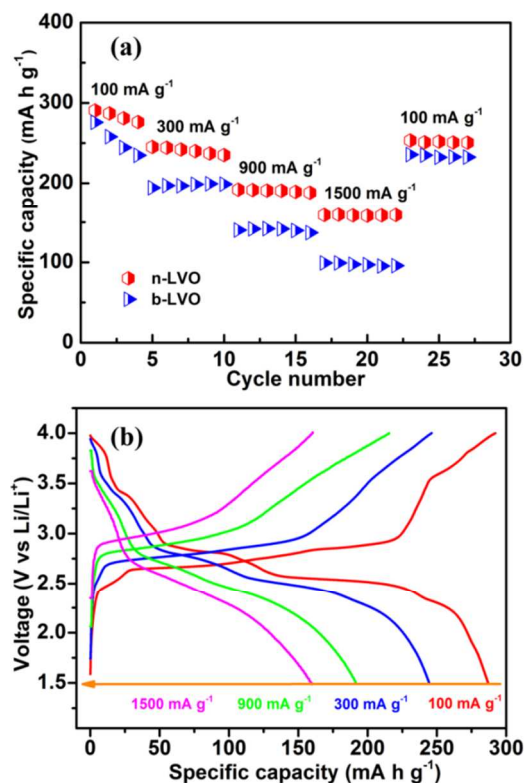
Fig. 9 (a) Rate-performance of n-LVO and b-LVO electrodes at various current densities from 100 to 1500 mA g^{-1}, and (b) discharge/charge

35 curves of n-LVO obtained at each rate.

below about 150 mA h g^{-1}.[14, 16-18, 45, 48] Furthermore, the reversible capacity of n-LVO is fairly stable at each rate, manifesting its prominent cycle reversibility and stability. By comparison, the b-LVO presents much lower reversible capacities of 275.8, 194,

40 140 and 99 mA h g^{-1} at current densities of 100, 300, 900 and 1500 mA g^{-1}, respectively. It is noticeable that the reversible capacities of b-LVO decrease by a large margin upon rate increasing, especially at the high rates of 900 and 1500 mA g^{-1}. Additionally, the charge/discharge curves of n-LVO at different

45 rates are shown in Fig. 9b. The well defined extraction/insertion plateaus at about 2.5 V become shorter upon rate increasing but persist throughout cycling, suggesting that no serious polarization has occurred. Aforementioned results have well substantiated the superior rate capability of the LiV_3O_8 nanorods over the bulk

50 counterpart.

    To the best of our knowledge, in spite of the remarkable capacity of the known LiV_3O_8 crystalline cathode, the long-term cycling performance at high current densities equal or greater than 2000 mA g^{-1} has rarely been studied. More surprising and

55 amazing results (as shown in Fig. 10) come from further studied high-rate capability of the n-LVO over prolonged cycling. It can be observed that the capacity *versus* cycle number curves obtained at 2000 and 3000 mA g^{-1} almost superimpose over each other. In other words, the n-LVO shows rather similar

60 electrochemical behavior at both high rates, and the reversible capacities over the long cycling merely decay slightly as the current density increases from 2000 to 3000 mA g^{-1}. The n-LVO can deliver appreciable initial reversible capacities of 161 and 158 mA h g^{-1} at the high rates of 2000 and 3000 mA g^{-1}, respectively.
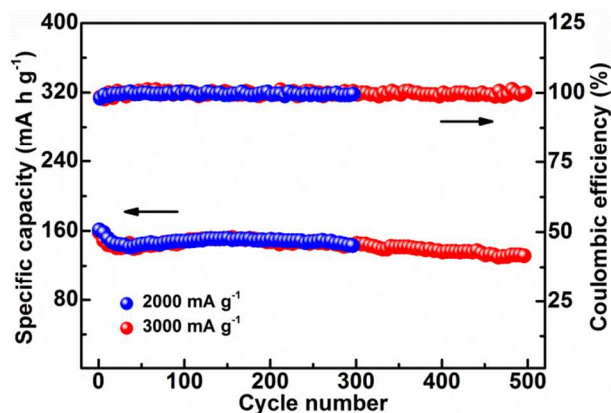
Fig. 10 High-rate performance of n-LVO electrode at high current densities of 2000 and 3000 mA g^{-1} upon long cycling.

It retains a reversible capacity of 143 mA h g^{-1} at 2000 mA g^{-1}
5 after 300 cycles, corresponding to a minimal decay rate of 0.037%

per cycle. Even after 500 extended cycles, the reversible capacity at 3000 mA g^{-1} can still sustain 133 mA h g^{-1}, representing an extremely low capacity fading of 0.031% per cycle. In the meantime, both of the coulombic efficiencies always
10 impressively approach 100% throughout the battery test, demonstrating the superb cycle reversibility of the n-LVO. Such long cycles with minimal capacity loss indicate the very long lifespan of the batteries. The reported Al$_2$O$_3$-coated LiV$_3$O$_8$ can deliver higher initial reversible specific capacities at current
15 densities of 2000 and 3000 mA g^{-1}, while its capacity retention falls to 71.3 and 74% after 100 cycles, respectively.[17] The hierarchical plate-arrayed LiV$_3$O$_8$ and nanosheets composite both exhibit exceptional capacity retention at 3000 mA g^{-1}, while deliver the initial reversible capacities less than 110 mA h g^{-1}.[46, 48]
20 Therefore, such prominent durable high-rate performances reported in our work reveal the potential of the LiV$_3$O$_8$ nanorods as cathodes in high-power and long-life rechargeable LIBs.

25 **Fig. 11** (a) Nyquist plots of the n-LVO and b-LVO electrodes, the inset represents the equivalent circuit. (b) Dependence of Z_{re} on the reciprocal square root of the frequency in the low-frequency region.

To gain a better insight into the rationales for the superior high-rate capability of our LiV$_3$O$_8$ nanorods, electrochemical impedance spectroscopy (EIS) measurements were carried out for
30 the n-LVO and b-LVO, as illustrated in Fig. 11. The Nyquist plots both display a compressed semicircle in the high to medium frequency range of each spectrum, which describes the charge transfer resistance, and a low frequency tail related to the diffusion of lithium ions in the solid matrix. The impedance
35 spectra can be well elucidated on the basis of the equivalent circuit shown in the insert of Fig. 11a, where the symbols, R_e, R_{ct}, CPE_{dl} and Z_w, stand for the solution resistance, charge transfer resistance, double layer capacitance and Warburg impedance, respectively. The fitted impedance parameters are listed in Table
40 S1.† Excellent correlation can be observed between the simulated curves and experimental data, indicating the accuracy of the circuit model within the experimental error limits. First to be point out that, both the R_e values are nearly identical due to the same electrolyte and fabrication processes. According to the
45 investigations into EIS of LIBs reported by Chen et al.,[49] the battery impedance primarily lies on cathode impedance,

especially charge transfer resistance. In the present work, the simulated R_{ct} value of n-LVO is remarkably less than that of b-LVO, signifying the substantially enhanced electron conduction
50 for n-LVO, which permits faster charge-transfer reaction for lithium-ion insertion and extraction in the electrode matrix.

It is generally accepted that the slanted lines in the low frequency range of EIS are attributed to the Warburg behavior, which should be associated with the lithium-ion diffusion within
55 the electrode matrix. And the solid-state diffusion of lithium-ion in active materials is considered to be the slowest process in lithium ion battery systems.[50] The apparent lithium-ion diffusion coefficient ($D_{apparent}$) can be estimated by using the following equation:[51]

60 $$D_{apparent} = (R^2 T^2)/(2A^2 n^4 F^4 C^2 \sigma^2) \quad (1)$$

where R is the gas constant, T is the absolute temperature, A is the surface area of the electrode, n is the number of electrons per molecule during oxidization, F is the Faraday constant, C is the concentration of lithium ions in the solid, and σ is the Warburg
65 factor relative to Z_{re} or Z_{im}.

$$Z_{re}(or -Z_{im}) \propto \sigma \omega^{-1/2} \quad (2)$$

On the basis of equation (2), the Warburg factor σ can be attained by linear fitting the relation plot between Z_{re} and the reciprocal square root of the angular frequency ω at the Warburg region (as shown in Fig. 11b). The apparent lithium-ion diffusion coefficient of n-LVO electrode is calculated to be approximately 5.5 folds of that of b-LVO electrode (as listed in Table S2†), indicating the drastically promoted lithium-ion diffusion kinetics in the former. In the case of solid-state diffusion of lithium ions in the electrode matrix, another important evaluation parameter is the diffusion time (τ_{eq}), which is proportional to the square of the average diffusion length. As previously mentioned, the lithium-ion diffusion length within the n-LVO is dramatically reduced owing to the nanometer size of electrode materials and the restricted preferential orientation of LiV_3O_8 nanocrystals. It is reasonable to infer that the mean diffusion time of n-LVO should be substantially shortened. Therefore, our LiV_3O_8 nanorods cathode can promptly absorb and store a vast number of lithium ions within a very short period, which should be energetically favorable for rapid charge and discharge.

Conclusion

In summary, LiV_3O_8 nanorods with confined preferential orientation have been successfully fabricated via a two-step route employing self-made $VO_2(B)$ nanosheets as the precursor. Compared to the bulk LiV_3O_8 materials made from commercial VO_2, much higher Li storage capacity, enhanced capacity retention abilities, significantly improved high-rate performance and impressive long-cycle stability have been attained for our LiV_3O_8 nanorods. A desirable initial reversible capacity of 200 mA h g^{-1} can be achieved at a moderately high rate of 600 mA g^{-1} with high capacity retention of 95% after 100 cycles. Moreover, the LiV_3O_8 nanorods amazingly present appreciable initial reversible capacities of 161 and 158 mA h g^{-1} at extremely high current densities of 2000 and 3000 mA g^{-1}, with minimal capacity loss of 0.037% and 0.031% per cycle over the lasting 300 and 500 cycles, respectively. The superior electrochemical properties of the LiV_3O_8 nanorods can be mainly ascribed to the energetically optimized electron conduction and lithium diffusion kinetics in electrode process contributed from the nanoscale grain size, large specific surface area and restricted preferential ordering along (100) plane. The results obtained in our work reveal the potential of our LiV_3O_8 nanorods as cathode materials for high-power and long-lifespan LIBs.

Acknowledgements

Notes and references

[a]Institute of Functional Materials, Department of Chemistry, Northeast Normal University, Changchun, Jilin 130024, P. R. China. E-mail: xinglong@nenu.edu.cn (XL), jpzhang@nenu.edu.cn (JP), wangrs@nenu.edu.cn (RS)

[b]National & Local United Engineering Lab for Power Battery, Northeast Normal University; Changchun, Jilin 130024, P.R. China.

† Electronic Supplementary Information (ESI) available: the additional Figures and Tables. For ESI or other electronic formats see DOI: 10.1039/b000000x.

1. J. Maier, *Nat. Mater.*, 2005, **4**, 805-815.
2. M. Winter and R. J. Brodd, *Chem. Rev.*, 2004, **104**, 4245-4270.
3. V. Etacheri, R. Marom, R. Elazari, G. Salitra and D. Aurbach, *Energy Environ. Sci.*, 2011, **4**, 3243.
4. P. G. Bruce, B. Scrosati and J. M. Tarascon, *Angew. Chem., Int. Ed.*, 2008, **47**, 2930-2946.
5. K. Kang, Y. S. Meng, J. Bréger, C. P. Grey and G. Ceder, *Science*, 2006, **311**, 977-980.
6. Y.-G. Guo, J.-S. Hu and L.-J. Wan, *Adv. Mater.*, 2008, **20**, 2878-2887.
7. X.-L. Wu, L.-Y. Jiang, F.-F. Cao, Y.-G. Guo and L.-J. Wan, *Adv. Mater.*, 2009, **21**, 2710-2714.
8. Y. G. Guo, Y. S. Hu, W. Sigle and J. Maier, *Adv. Mater.*, 2007, **19**, 2087-2091.
9. M. Winter, J. O. Besenhard, M. E. Spahr and P. Novák, *Adv. Mater.*, 1998, **10**, 725-763.
10. L. Jiao, L. Liu, J. Sun, L. Yang, Y. Zhang, H. Yuan, Y. Wang and X. Zhou, *J. Phys. Chem. C*, 2008, **112**, 18249-18254.
11. H. Liu, Y. Wang, K. Wang, Y. Wang and H. Zhou, *J. Power Sources*, 2009, **192**, 668-673.
12. A. Pan, J. Liu, J.-G. Zhang, G. Cao, W. Xu, Z. Nie, X. Jie, D. Choi, B. W. Arey, C. Wang and S. Liang, *J. Mater. Chem.*, 2011, **21**, 1153.
13. H. Liu, Y. Wang, W. Yang and H. Zhou, *Electrochim. Acta*, 2011, **56**, 1392-1398.
14. H. Wang, Y. Ren, Y. Wang, W. Wang and S. Liu, *CrystEngComm*, 2012, **14**, 2831.
15. X. Xu, Y.-Z. Luo, L.-Q. Mai, Y.-L. Zhao, Q.-Y. An, L. Xu, F. Hu, L. Zhang and Q.-J. Zhang, *NPG Asia Mater.*, 2012, **4**, e20.
16. R. Mo, Y. Du, N. Zhang, D. Rooney and K. Sun, *Chem. Commun.*, 2013, **49**, 9143-9145.
17. S. Huang, J. P. Tu, X. M. Jian, Y. Lu, S. J. Shi, X. Y. Zhao, T. Q. Wang, X. L. Wang and C. D. Gu, *J. Power Sources*, 2014, **245**, 698-705.
18. Y. Liu, X. Zhou and Y. Guo, *Electrochim. Acta*, 2009, **54**, 3184-3190.
19. S. Sarkar, H. Banda and S. Mitra, *Electrochim. Acta*, 2013, **99**, 242-252.
20. G. Yang, G. Wang and W. Hou, *J. Phys. Chem. B*, 2005, **109**, 11186-11196.
21. N. Tran, K. G. Bramnik, H. Hibst, J. Prölß, N. Mronga, M. Holzapfel, W. Scheifele and P. Novák, *J. Electrochem. Soc.*, 2008, **155**, A384-A389.
22. Y. Feng, F. Hou and Y. Li, *J. Power Sources*, 2009, **192**, 708-713.
23. H. Y. Xu, H. Wang, Z. Q. Song, Y. W. Wang, H. Yan and M. Yoshimura, *Electrochim. Acta*, 2004, **49**, 349-353.
24. Y. Liu, X. Zhou and Y. Guo, *J. Power Sources*, 2008, **184**, 303-307.
25. A. Pan, J.-G. Zhang, G. Cao, S. Liang, C. Wang, Z. Nie, B. W. Arey, W. Xu, D. Liu, J. Xiao, G. Li and J. Liu, *J. Mater. Chem.*, 2011, **21**, 10077.
26. J. Liu, W. Liu, Y. Wan, S. Ji, J. Wang and Y. Zhou, *RSC Adv.*, 2012, **2**, 10470.
27. A. S. Arico, P. Bruce, B. Scrosati, J.-M. Tarascon and W. van Schalkwijk, *Nat. Mater.*, 2005, **4**, 366-377.
28. Y. Wang and G. Cao, *Adv. Mater.*, 2008, **20**, 2251-2269.
29. M. G. Kim and J. Cho, *Adv. Funct. Mater.*, 2009, **19**, 1497-1514.
30. L. A. de Picciotto, K. T. Adendorff, D. C. Liles and M. M. Thackeray, *Solid State Ionics*, 1993, **62**, 297-307.
31. Y. Gu, D. Chen, X. Jiao and F. Liu, *J. Mater. Chem.*, 2006, **16**, 4361-4366.
32. L. Jiao, H. Li, H. Yuan and Y. Wang, *Mater. Lett.*, 2008, **62**, 3937-3939.
33. J. Sun, L. Jiao, H. Yuan, L. Liu, X. Wei, Y. Miao, L. Yang and Y. Wang, *J. Alloys Compd.*, 2009, **472**, 363-366.
34. K. West, B. Zachau‐Christiansen, S. Skaarup, Y. Saidi, J. Barker, I. I. Olsen, R. Pynenburg and R. Koksbang, *J. Electrochem. Soc.*, 1996, **143**, 820-825.
35. M. Okubo, E. Hosono, J. Kim, M. Enomoto, N. Kojima, T. Kudo, H. Zhou and I. Honma, *J. Am. Chem. Soc.*, 2007, **129**, 7444-7452.

36. J. Chen and F. Cheng, *Acc. Chem. Res.*, 2009, **42**, 713-723.
37. C. Q. Feng, L. F. Huang, Z. P. Guo, J. Z. Wang and H. K. Liu, *J. Power Sources*, 2007, **174**, 548-551.
38. Y. Liu, X. Zhou and Y. Guo, *Mater. Chem. Phys.*, 2009, **114**, 915-919.
39. G. Pistoia, M. Pasquali, G. Wang and L. Li, *J. Electrochem. Soc.*, 1990, **137**, 2365-2370.
40. M. Zhao, L. Jiao, H. Yuan, Y. Feng and M. Zhang, *Solid State Ionics*, 2007, **178**, 387-391.
41. L. Liu, L. Jiao, J. Sun, M. Zhao, Y. Zhang, H. Yuan and Y. Wang, *Solid State Ionics*, 2008, **178**, 1756-1761.
42. X.-L. Wu, Y.-G. Guo, J. Su, J.-W. Xiong, Y.-L. Zhang and L.-J. Wan, *Adv. Energy Mater.*, 2013, **3**, 1155-1160.
43. H. Guo, L. Liu, Q. Wei, H. Shu, X. Yang, Z. Yang, M. Zhou, J. Tan, Z. Yan and X. Wang, *Electrochim. Acta*, 2013, **94**, 113-123.
44. L. Liu, F. Tian, X. Wang, Z. Yang and X. Wang, *Ionics*, 2012, **19**, 9-15.
45. S. Huang, X. L. Wang, Y. Lu, X. M. Jian, X. Y. Zhao, H. Tang, J. B. Cai, C. D. Gu and J. P. Tu, *J. Alloys Compd.*, 2014, **584**, 41-46.
46. S. Huang, Y. Lu, T. Q. Wang, C. D. Gu, X. L. Wang and J. P. Tu, *J. Power Sources*, 2013, **235**, 256-264.
47. H.-L. Zhang, J. R. Neilson and D. E. Morse, *J. Phys. Chem. C*, 2010, **114**, 19550-19555.
48. N. H. Idris, M. M. Rahman, J.-Z. Wang, Z.-X. Chen and H.-K. Liu, *Compos. Sci. Technol.*, 2011, **71**, 343-349.
49. C. H. Chen, J. Liu and K. Amine, *J. Power Sources*, 2001, **96**, 321-328.
50. S. Lee, Y. Cho, H. K. Song, K. T. Lee and J. Cho, *Angew. Chem., Int. Ed.*, 2012, **51**, 8748-8752.
51. C. J. Wen, C. Ho, B. A. Boukamp, I. D. Raistrick, W. Weppner and R. A. Huggins, *Int. Mater. Rev.*, 1981, **26**, 253-268.

RSC Advances Accepted Manuscript

TOC
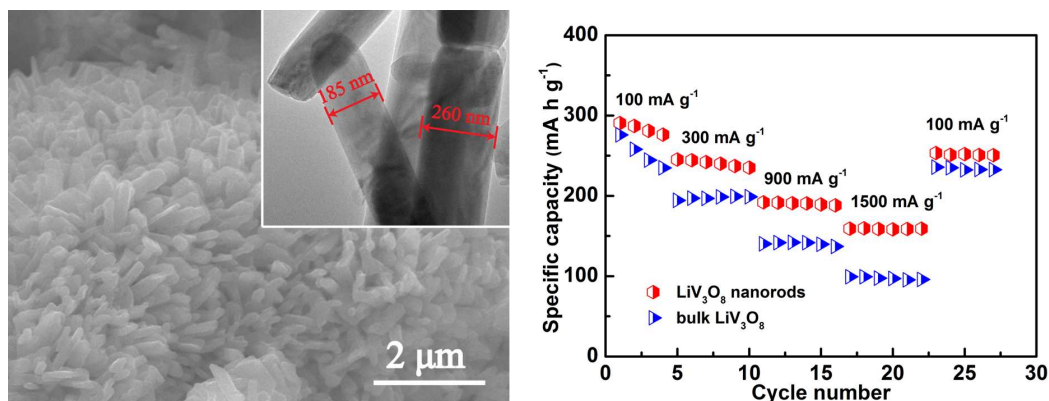
Much enhanced reversible capacities and capacity retention abilities, significantly improved high-rate performance and long-term stability have been attained for LiV_3O_8 nanorods synthesized by a two-step route using self-made $VO_2(B)$ as the precursor.